Contents lists available at ScienceDirect

Applied Catalysis B: Environment and Energy

Boosting hydrogen evolution performance of nanoporous Fe-Pd alloy electrocatalyst by metastable phase engineering

Zhangyi Li [a], Chaoyang Wang [a,c], Yanqin Liang [a,b], Hui Jiang [a,b], Shuilin Wu [a], Zhaoyang Li [a,b], Wence Xu [a,*], Shengli Zhu [a,b,**], Zhenduo Cui [a,*]

[a] *School of Materials Science and Engineering, Tianjin University, Tianjin 300350, China*
[b] *Tianjin Key Laboratory of Composite and Functional Materials, Tianjin 300350, China*
[c] *School of Mechanical Engineering, Dongguan University of Technology, Dongguan 523808, China*

ARTICLE INFO

ABSTRACT

Nanoporous Fe-Pd alloy with metastable face-centered cubic (fcc Fe-Pd) phase is prepared by electrochemical dealloying as an electrocatalyst for hydrogen evolution reaction (HER). The nanoporous fcc Fe-Pd alloy achieves an overpotential of 58 mV at 10 mA cm^{-2} in 1 M KOH, outperforming those of stable body-centered cubic Fe-Pd alloy (bcc Fe-Pd) and commercial Pt/C catalyst. Density functional theory calculation reveals that the metastable fcc structure can tailor the coordination environment and electronic structure of Pd active sites in Fe-Pd alloy. As a result, the d-band center of Pd active site shifts away from the Fermi level, which weakens the Pd-H interaction and reduces the energy barrier of water dissociation. In addition, the fcc Fe-Pd exhibits good mechanical properties, which maintains the catalytic performance in the deformation state. This work broadens the idea for designing and preparing HER catalysts via metastable phase structure design.

1. Introduction

Clean and renewable hydrogen energy is an appropriate candidate for substituting fossil energies [1–4]. Electrocatalytic hydrogen evolution reaction (HER) is a promising method for hydrogen production due to the high efficiency, simplicity, environmental friendly and carbon-free emission [5–7]. In industrial processes, the alkaline water electrolysis system presents an attractive opportunity for stabilizing the HER setup and enabling the exploration of new catalytic materials with earth-abundant elements [8,9]. However, the production of hydrogen in alkaline water is still challenging due to the high energy barrier for water dissociation and the inadequate release of hydrogen [10,11]. Moreover, noble metal-based catalysts are still the best catalysts for HER, but the high cost and scarcity limit their industrial application [12]. Great efforts have been devoted to the development of high-performance electrocatalysts for alkaline HER. Nevertheless, there is still an urgent need for developing new catalytic materials with high activity, stability, and low resource consumption [13,14].

Recent studies suggest that metastable phase catalysts possess high catalytic activity for HER due to their unique electronic structure and

non-equilibrium metal surface with high energy structure [15,16]. However, synthesizing metastable materials is difficult due to their high susceptibility to phase transitions from high-energy to low-energy structures [17]. Alloying is an effective method for improving the thermodynamic stability of metastable materials in which atoms with larger radius to stabilize the loosely packed atoms [18,19]. Transition metals possess more diverse crystal phases, for example, both fcc and bcc phases can be found in Fe, which can expand the synthesis of metastable-phase transition metal alloys. Furthermore, the addition of a small amount of noble metal to a transition metal matrix can stabilize the transition metal atoms in the metastable phase during thermodynamic transformation [20]. In addition, it has been demonstrated that alloying is an efficient strategy for tuning the electronic and geometric features of noble metal active centers [21]. Noble metals typically have high electron affinity and electronegativity, which can attract and polarize neighboring transition metal atoms and ligands, adjust electron density and distribution, leading to an optimizing of the Fermi Level in the noble metal atoms [22–24]. Additionally, the mismatching atomic radius between transition metals and noble metals can induce significant strains in the alloy phase, leading to the broaden of d-band and

---

regulation of the d-band center position [25]. In addition, palladium (Pd)-based nanomaterials are considered as good candidates for hydrogen evolution (HER) due to their similar characters with platinum (Pt), such as encompassing phase structure, atomic size, and electronic configuration [26,27]. Therefore, it is promising to improve the HER catalytic activity of Pd-based alloy by optimizing the electronic structure and coordination environment via metastable phase engineering.

In this work, nanoporous metastable fcc Fe-Pd alloy prepared by electrochemical dealloying is proposed as an efficient electrocatalyst for HER in alkaline electrolyte. The metastable fcc Fe-Pd exhibits an overpotential of 58 mV at a current density of 10 mA cm^{-2}, which outperforms the stable bcc Fe-Pd and commercial Pt/C catalyst. Density functional theoretical (DFT) analysis confirms that the metastable phase engineering enhances the charge density and electronic states of Pd active site, thereby reducing the energy barriers associated with water adsorption and dissociation. The remarkable mechanical properties ensure a consistent hydrogen evolution ability in the deformation state. This study provides insights into the development of highly efficient HER electrocatalysts based on metastable alloys.

2. Experimental section

2.1. Chemicals and materials

Phosphoric acid (H$_3$PO$_4$, AR, 85 wt%) was purchased from Meryer Biochemical (Shanghai) Technology Co., Ltd. Potassium hydroxide (KOH, AR, 99.5 wt%) was purchased from Komeo Chemical Reagent (Tianjin) Co., Ltd. Iron (Fe, 99.95 wt%), palladium (Pd, 99.95 wt%), Niobium (Nb, 99.95 wt%) and boron (B, 99.95 wt%) were from ZhongNuo Advanced Material (Beijing) technology Co., Ltd. Pt/C catalyst (20 wt% Pt on Vulcan XC-72R carbon) and Pd/C catalyst (20 wt% Pt on Vulcan XC-72R carbon) were from Heowns Biochem Technologies LLC, Tianjin, China. Isopropyl alcohol (99.9 wt%) and Nafion (5 wt%) were obtained from Sigma-Aldrich Chemical Reagent Co., Ltd. Other materials were obtained from commercial suppliers and used without further purification. The water used in all experiments was purified through a Millipore system.

2.2. Preparation of Precursor ribbons

Alloy ingots with nominal atomic composition of Fe$_{82}$Nb$_6$B$_{12}$ and Fe$_{80}$Nb$_6$B$_{12}$Pd$_2$ were prepared by arc-melting the mixtures of pure elements under argon atmosphere. The ingots were re-melted by a high-frequency induction furnace in a quartz nozzle and then rapidly ejected onto a rotating copper wheel with a circumferential velocity of 26.2 m s^{-1} [28,29]. The size of as-spun alloy ribbon was 25 μm in thickness and 1.5 mm in width.

2.3. Synthesis of nanoporous Fe-Pd alloys

The ribbon was used as precursor to produce nanoporous electrode by potentiostatic etching. The potentiostatic etching were carried out in a three-electrode system, in which the Ag/AgCl electrode, Pt sheet and precursor alloy were served as the reference electrode, counter electrode, working electrode, respectively. The potentiodynamic polarization measurement of the precursor alloy ribbon at 0.3 mol L^{-1} H$_3$PO$_4$ was used to determine suitable etching potentials for selective phase dissolution.

The two nanoporous samples were chosen for the following characterization and properties test: 1) bcc Fe-Pd: dealloying the Fe-Pd alloy precursor for 600 s under − 0.15 V (vs. Ag/AgCl); 2) fcc Fe-Pd: dealloying the Fe-Pd alloy precursor for 600 s under − 0.21 V (vs. Ag/AgCl). 3) bcc Fe: dealloying the Fe alloy precursor for 600 s under − 0.15 V (vs. Ag/AgCl).

2.4. Materials characterization

Phases composition was determined by X-ray diffraction (XRD: Bruker D8) with Cu Kα radiation. The morphology, microstructure and chemical composition were examined using a transmission electron microscope (TEM: JEOL JEM-2100 F) and scanning electron microscope (SEM: Hitachi S-4800) equipped with energy dispersive X-ray spectroscope (EDS). The element valence was analyzed by X-ray photoelectron spectroscope (XPS; Axis Supra). The Pd concentrations in specimens were determined by inductively coupled plasma optical emission spectroscopy (ICP-OES) with an ICP-OES 730 instrument. The micromechanical properties of the samples were measured by nanomechanics measurement system(Hysitron TI-Premier). The tensile mechanical properties of the samples were measured by a micro-controlled electronic universal testing machine (WDW-20).

2.5. Electrochemical measurements

A Gamry Interface 1000 electrochemical workstation was used to perform the electrochemical measurements with a typical three electrode system. The Ag/AgCl electrode, Pt sheet and as-prepared sample were served as the reference electrode, counter electrode, working electrode, respectively. The HER performance was measured in 1.0 mol L^{-1} of KOH electrolyte with N$_2$ purification at room temperature. The test potentials vs. the Ag/AgCl electrode were converted to the potentials vs. reversible hydrogen electrode (RHE) using Nernst equation. A series of electrochemical tests, such as linear sweep voltammetry (LSV), Tafel plot analysis, electrochemical impedance spectroscopy (EIS), cyclic voltammetry (CV), electrochemically active surface area (ECSA), and chronopotentiometry (CP), were conducted to investigate the performance of nanoporous catalysts in the HER process.

2.6. Electrochemical calculation

For the electrocatalytic redox reaction, the applied potential can be expressed by the Nernst equation (Eq. 1) [30].

$$E = E^0 + \frac{RT}{nF}\ln\left(\frac{C_0}{C_R}\right) \tag{1}$$

where E is the applied potential, E^0 is the standard potential, R is the universal gas constant, T is the absolute temperature, F is the Faraday constant, and C_O and C_R are the concentrations of oxidized and reduced reagents, respectively.

Overpotential (η) can be represented by Eq. (2),

$$\eta = E - E_{eq} \tag{2}$$

For water electrolysis, the overpotential (η) reported in the literature is at the benchmark current density of 10 mA cm^{-2}, where E_{eq} is the equilibrium potential [31]. For the polarization measurements, the scan rate was 5 mV s-1, and the test temperature was 25 °C. All the potentials were calculated to the reversible hydrogen electrode (RHE) according to the Eq. (3).

$$E_{(RHE)} = E_{(Ag/AgCl)} + 0.1989 + 0.059 \times 14 \tag{3}$$

The potentials were further iR-compensated according to the following Eq. (4):

$$E_{corr} = E_{mea} - iR_s \tag{4}$$

where E_{corr} is the *iR*-compensated potential, E_{mea} is the measured potential, i is the current and R_s is the equivalent series resistance measured by electrochemical impedance spectroscopy (EIS). EIS measurements were carried out at an overpotential of 150 mV. The frequency range of the EIS measurement is from 100000 Hz to 0.1 Hz at a perturbation AC voltage of 10 mV.

The Tafel slope describes the relationship between steady-state cur-

rent density and overpotential, and it can be expressed by Eq. (5).

$$\eta = a + b\log(j) \tag{5}$$

where b is the Tafel slope, j is the exchange current density.

The double layer capacitance (Cdl) is calculated through a process that involves recording multiple cyclic voltammetry (CV) scans in a non-faradaic region, using a certain potential window at varying scan rates (typically 10–200 mV s^{-1}). The cathodic and anodic current density variation ($\Delta J = J_a - J_c$) at an overpotential is then determined, and the resulting differences are plotted against the scan rates. These plotted lines are then subjected to linear regression analysis, which enables the determination of Cdl. Specifically, the slope of the fitted line is twice the value of Cdl [32].

The values of ECSA of each catalyst was calculated according to the following Eq. (6):

$$ECSA = \frac{C_{dl}}{C_s} \tag{6}$$

where C_s is the specific capacitance of the sample and is estimated to be 40 μF cm^{-2} according to previous work [33].

The Turnover frequency (TOF) is defined as the number of molecules generated catalytically per catalytic site per second, and it can be calculated using the following Eq. (7) [32]:

$$TOF = \frac{jA}{2Fn} \tag{7}$$

Where the j refers to the current density (A cm^{-2}) at a specific over-potential, A denotes the area of the electrode (cm^{-2}), F is the Faraday constant (96 485 C mol^{-1}), and n represents the concentration of active sites in the catalyst (mol cm^{-2}).

Mass activity(MA) was obtained by normalizing the current density to the load mass of the electrocatalyst, which can be expressed by Eq. (8) [34],

$$MA = \frac{j}{m} \tag{8}$$

where j is the measured current density (mA cm^{-2}), and m is the mass loading (mg cm^{-2}) of the working electrode.

The specific activity is estimated by normalizing the current density to the active surface area of the electrocatalyst (Eq. 9) [34].

$$SA = \frac{MA}{ECSA} \tag{9}$$

2.7. DFT calculations

We have employed the first principles to perform density functional theory (DFT) calculations within the generalized gradient approximation (GGA) using the Perdew-Burke-Brinkerhoff (PBE) formulation. We have chosen the projected augmented wave (PAW) potentials [35] to describe the ionic cores and take valence electrons into account using a plane wave basis set with a kinetic energy cutoff of 400 eV. Partial occupancies of the Kohn−Sham orbitals were allowed using the Gaussian smearing method and a width of 0.05 eV. The electronic energy was considered self-consistent when the energy change was smaller than 10^{-6} eV. A geometry optimization was considered convergent when the energy change was smaller than 0.05 eV Å^{-1}. The vacuum spacing in a direction perpendicular to the plane of the structure is 18 Å for the surfaces. The Brillouin zone integration is performed using $3 \times 3 \times 1$ Monkhorst-Pack k-point sampling for a structure. Finally, the adsorption energies(E_{ads}) were calculated as $E_{ads} = E_{ad/sub} - E_{ad} - E_{sub}$, where $E_{ad/sub}$, E_{ad}, and E_{sub} are the total energies of the optimized adsorbate/substrate system, the adsorbate in the structure, and the clean substrate, respectively. The free energy was calculated using the Eq. (10):

$$G = E_{ads} + ZPE - TS \tag{10}$$

where G, Eads, ZPE and TS are the free energy, total energy from DFT calculations, zero-point energy and entropic contributions, respectively.

3. Results and discussion

Fig. 1a schematically illustrates the synthetic route of nanoporous Fe-Pd alloy electrode. The Fe-Pd alloy precursor ribbon was prepared by melt-spinning. Steady bcc phase and metastable fcc phase can be detected by X-ray diffraction (XRD, Fig. S1) [36,37]. The diffraction peaks of both crystalline phases shift to lower angle region compared with metallic bcc Fe, indicating the partial substitution of Fe atoms by the larger Pd atoms [38]. The existence of metastable fcc phase can be attributed to the addition of restricted diffusion Pd element, which can promote the formation of fcc phase in a wider range of compositions [36]. The nanoporous Fe-Pd alloys were further prepared by electrochemical dealloying, the crystal structure of the nanoporous layer can be tuned by controlling the applied potentials due to the difference in electrochemical stability between bcc phase and fcc phase. Fig. S2 shows the phase etching process of precursor ribbons at different potentials. At low dealloying potential, active bcc phase was selectively etched from the precursor alloy, forming the nanoporous fcc Fe-Pd alloy. At high dealloying potential, both fcc and bcc are simultaneously dissolved. The fcc phase would leach out completely due to the relative lower content in the precursor alloy and the bcc phase would be partially remained.

As displayed in Fig. 1b, XRD patterns of the samples present fcc and bcc phases respectively, verifying the crystal structure can be controlled by dealloying potential. Fig. 1c and Fig. S3 reveal similar nanoporous structures with interconnected pores and ligaments, the pore sizes of the fcc Fe-Pd, bcc Fe-Pd and bcc Fe are approximately 100 nm. As shown in Fig. S4, the thickness of the nanoporous layer gradually increases with prolonged etching time. The nanoporous layer possesses a thickness of approximately 1100 nm after 600 s of dealloying, and it remains relatively constant beyond 600 s of etching. Table S2 shows the energy dispersive spectroscopy (EDS) result of the fcc Fe-Pd and bcc Fe-Pd. The atomic ratio of Fe:Pd of fcc Fe-Pd is 6.4:1, which is similar to that of bcc Fe-Pd (6.8:1). The phase composition and nanostructure of fcc Fe-Pd is further illustrated by TEM. As shown in Fig. 1d, the ligament size of fcc Fe-Pd is about 30 nm, which is in accordance with the SEM image in Fig. 1c. High-resolution TEM (HRTEM) image of fcc Fe-Pd (Fig. 1e) exhibits the nano-sized crystalline phase with an intergranular spacings of 0.19 and 0.22 nm, which are ascribed to the (200) and (111) crystal planes of fcc Fe-Pd, respectively. The spacings are larger than those of the theoretical value for pure fcc Fe (0.18 and 0.21 nm), implying the substitution of Pd atoms in the Fe lattice sites. The selected area electron diffraction pattern (SAED, Fig. 1f) further suggests the fcc Fe-Pd ligaments are composed of small nanocrystals. In addition, bcc Fe-Pd possesses similar microstructure compared with fcc Fe-Pd with the crystal structure of bcc phase (Fig. S5). Furthermore, the corresponding EDS mapping images show the uniform distribution of Fe and Pd atoms (Fig. 1g).

X-ray photoelectron spectroscopy (XPS) was applied to investigate the surface chemical states of the as-prepared catalysts. As shown in Fig. S6a, The Fe 2p$_{3/2}$ peaks at 711.0 eV and 713.6 eV can be attributed to the surface oxidation of Fe and the peaks at 706.8 eV can be attributed to the Fe^0 [39]. The Pd 3d$_{5/2}$ peaks at 335.3 eV is assigned to Pd^0 and the peak at 337.2 eV is the feature of Pd^{2+} due to surface oxidation when exposing in the circumambient environment (Fig. S6b) [29]. In addition, the Pd^0 3d peaks of fcc Fe-Pd shift negatively and the peaks of Fe^0 shift positively compared with bcc Fe-Pd, indicating that more electrons on Fe transfer to Pd in the metastable fcc alloy phase. The shift of binding energy indicates that the metastable state promotes the electronic localization of Pd and the electron donating ability of Fe, which is expected to benefit the electrocatalysis [40,41].
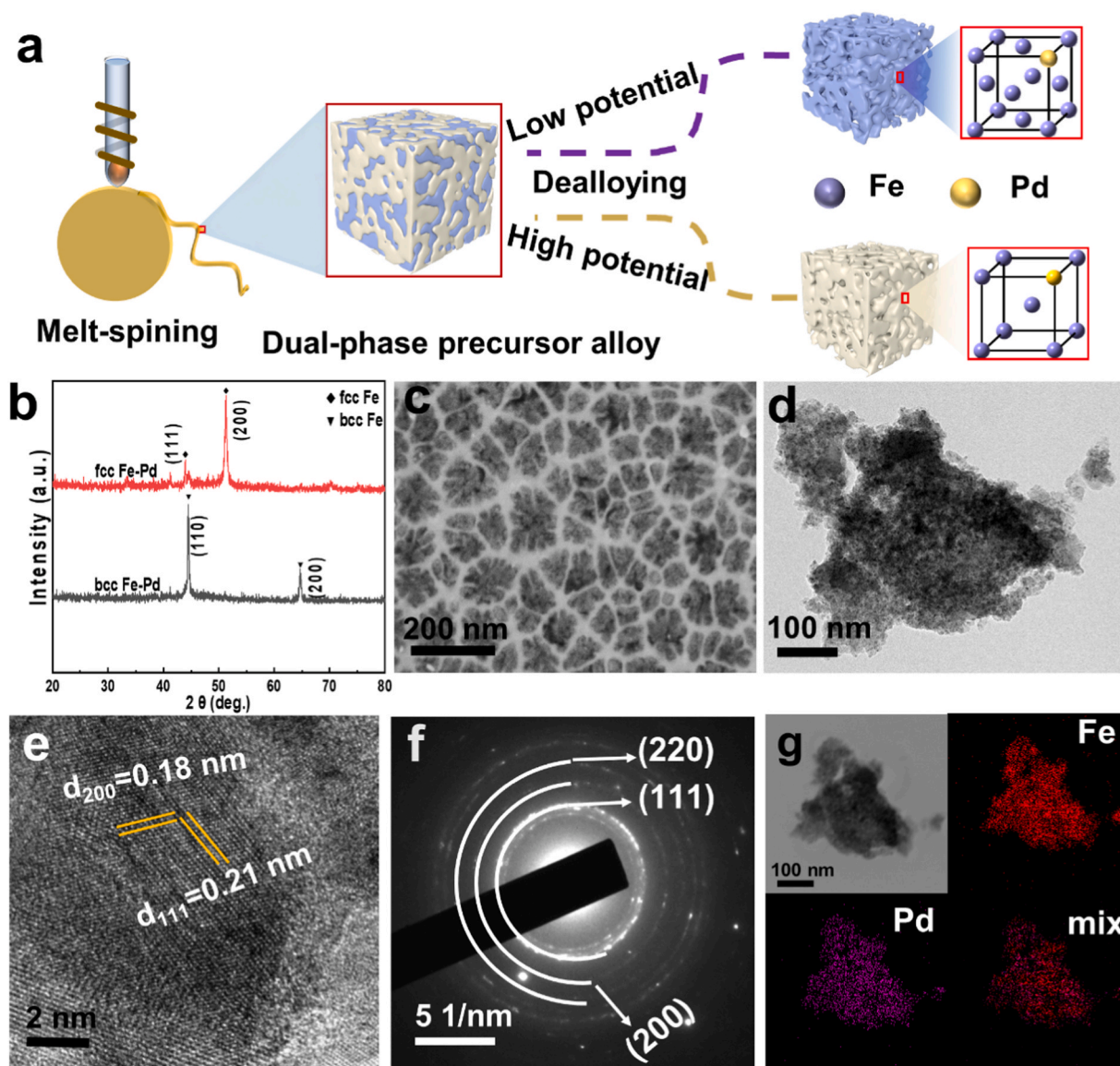
Fig. 1. Preparation and characterization of nanoporous Fe-Pd ribbons a). Schematic illustration of Fe based nanopores with adjustable phase formed through electrochemical dealloying strategy. b) XRD patterns of nanoporous Fe-Pd samples. c) Scanning electron microscope images of the surface of fcc Fe-Pd samples. d- e) Bright-field TEM images and high-resolution TEM image. f) The selected area electron diffraction pattern (SAED). g) The corresponding energy dispersive X-ray spectroscopy (EDS) mapping images of fcc Fe-Pd.

The electrocatalytic performances of the nanoporous Fe-Pd alloys were measured by a typical three-electrode electrochemical cell in 1 M KOH solution. As displayed in Fig. 2a, the fcc Fe-Pd exhibits an over-potential of 58 mV at a current density of 10 mA cm^{-2}, which is lower than those of bcc Fe (337 mV), bcc Fe-Pd (191 mV), commercial Pd/C catalyst (114 mV) and commercial Pt/C catalyst (70 mV). In addition, the fcc Fe-Pd delivers lower HER overpotentials at high current densities, demonstrating the potentiality of fcc Fe-Pd for industrial applications (Fig. 2b). Fig. S7 shows that the precursor ribbon exhibits poor HER activity, while with the increasing of dealloying time, the nanoporous samples exhibit significantly improved HER activity. This is due to the higher specific surface area of the nanoporous structure, which plays a key role in exposing more active sites. At the same time, this feature increases the contact frequency between the solution medium and the active sites, ultimately improving the overall efficiency of the HER [2,42,43]. When the etching time is less than 600 s, the performance increases with the increase of dealloying time, which is due to the exposure of more active sites. When the etching time is 600 s, the sample

shows the best performance. When the etching time further increases to 1200 s, the performance decreases gradually, which is due to the dissolution of part of the active phase. At the same etching time, the HER performance of fcc Fe-Pd sample is much better than that of bcc Fe-Pd sample, primarily due to the dominant impact of metastable phase. The above results highlight a significant improvement in the HER performance of Pd when utilized as the active center within the metastable structure, emphasizing its potential for commercialization.

The generally accepted model for the basic HER process involves a formation step where hydrogen species are adsorbed ($H_2O + e^- \rightarrow H_{ad} + OH^-$, Volmer step) and a desorption step where adsorbed hydrogen combines to form hydrogen molecules ($H_{ad} + H_2O + e^- \rightarrow H_2 + OH^-$, Heyrovsky step, or $2\,H_{ad} + 2e^- \rightarrow H_2$, Tafel step) [7,44]. As evidenced in Fig. 2c, the bcc Fe-Pd exhibits a Tafel slope of 136 mV dec^{-1}, indicating the bcc Fe-Pd follows Volmer process as the rate-determining step [45]. In addition, the fcc Fe-Pd possesses lower Tafel slope of 88 mV dec^{-1} compared with the bcc Fe-Pd, indicating improved water dissociation kinetics for HER. Fig. 2d and Table S3 illustrate the HER performance of
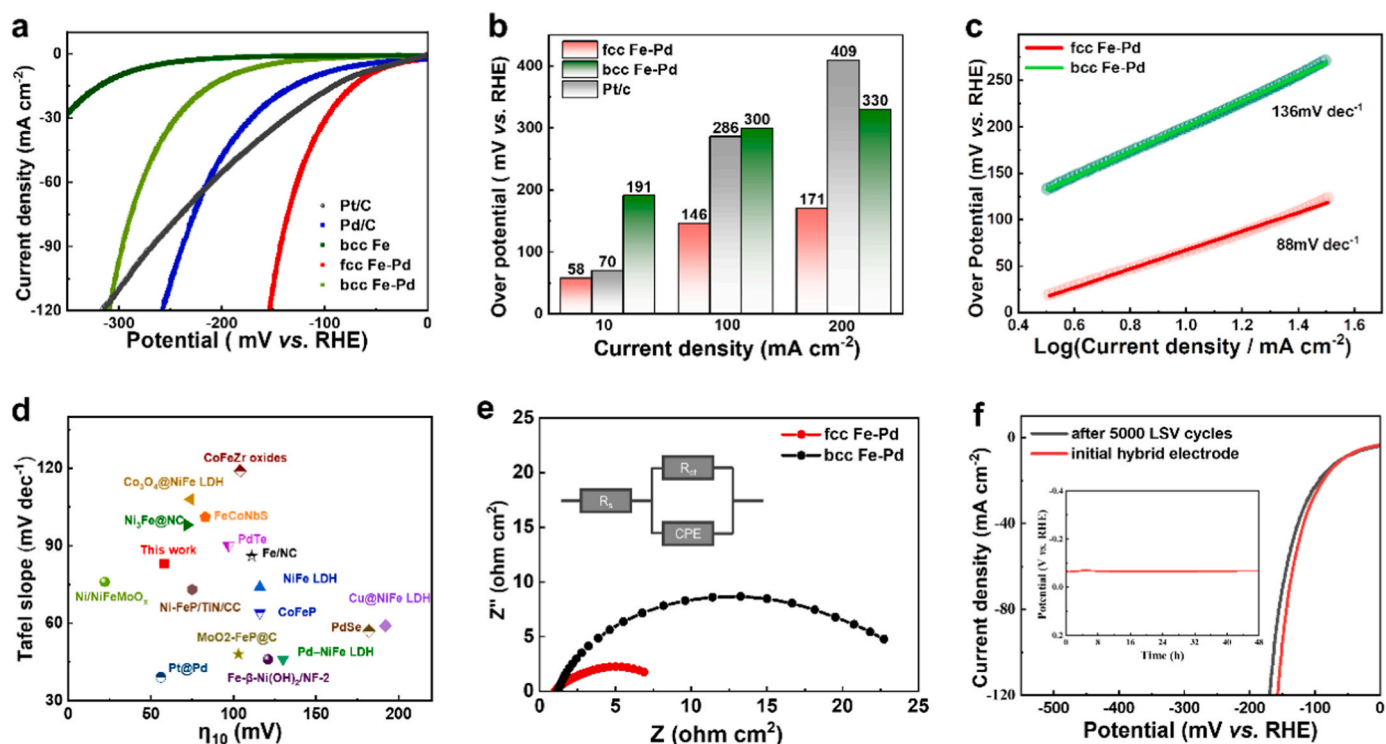
Fig. 2. HER electrocatalytic performance of nanoporous Fe-Pd alloys in 1 M KOH solution. a) Linear sweep voltammetry polarization (LSV) curves. b) Overpotential of fcc Fe-Pd at different current densities. c) Tafel plots of fcc Fe-Pd and bcc Fe-Pd. d) Overpotential and Tafel slope comparison with other Fe-base or Pd-base electrocatalysts driven with η_{10}. e) Nyquist plots for different electrodes in 1 M KOH. f) HER polarization curves of fcc Fe-Pd before and after 5000 cycle tests. The illustration shows that the time-dependent HER stability of the fcc Fe-Pd over 48 h at a current density of 10 mA cm^{-2} in 1.0 m KOH solutions.

the fcc Fe-Pd in comparison to other HER catalysts, the fcc Fe-Pd exhibits outstanding performance and demonstrates its potential as a highly efficient catalyst for HER.

The charge transfer resistance of the nanoporous Fe-Pd alloys were investigated by electrochemical impedance spectroscopy (EIS). The fitted Nyquist plots and an appropriate equivalent circuit diagram are shown in Fig. 2e. The equivalent circuit consists of a solution resistance (R_s), a charge-transfer resistance (R_{ct}), and a constant phase element (CPE). As evidenced in Table S3, the fcc Fe-Pd delivers a smaller R_{ct} value of 8.04 Ω cm^2 compared with bcc Fe-Pd (22.98 Ω cm^2), indicating the improved electron transport rate and catalytic kinetics for fcc Fe-Pd [46,47]. The number of active sites were measured by electrochemical surface area (ECSA). As displayed in Fig. S8 and Fig. S9, fcc Fe-Pd exhibits higher ECSA value than bcc Fe-Pd, indicating the more active sites can be exposed on the surface of the metastable fcc crystal structure. The intrinsic catalytic activities of the as-prepared catalysts were further evaluated by measuring the turnover frequency (TOF), specific activity (SA) and mass activity (MA) (Fig. S10). It is evident that the fcc Fe-Pd exhibits a distinct advantage in terms of intrinsic activity compared with the bcc Fe-Pd. As depicted in the Fig. S11, the corresponding LSV plots for TOF(a), MA(b) and SA(c) have been provided. The intrinsic activity of fcc Fe-Pd surpasses that of bcc Fe-Pd across all potential intervals. The superior catalytic activity of fcc Fe-Pd can be attributed to the fasten charge transfer, increase of active sites and improved intrinsic catalytic activity caused by the existence of metastable fcc Fe-Pd phase.

Long-term stability was examined by the chronopotentiometry and cyclic LSV tests. As shown in Fig. 2f, the fcc Fe-Pd shows negligible activity loss for 48 h at 10 mA cm^{-2}. In addition, no significant change of the morphology and composition can be seen after stability test, verifying good catalytic stability of fcc Fe-Pd (Fig. S12). The XRD (Fig. S13) results demonstrate that the fcc phase is stable after an extended period of stability testing. Concurrently, the XPS results (Fig. S14) reveal a weakening of the Fe^0 peak after the stability test,

indicating the inevitable oxidation of Fe in the electrolyte. The illustration in Fig. 2f shows the LSV curves of the fcc Fe-Pd before and after 5000 cycles test. There is only slight degradation at high current density, verifying good stability of fcc Fe-Pd. The industrial water electrolysis is usually carried out at the high current density, hence the HER stability at high current should be very important. As depicted in Fig. S15, at a current density of 1 A cm^{-2}, the performance exhibited minimal degradation even after 48 h of testing. The above results demonstrate the excellent potential of fcc Fe-Pd for HER under alkaline condition.

To get further insight into the HER mechanism on the Fe-Pd alloys, density functional theory (DFT) calculations were performed, the optimized fcc Fe-Pd and bcc Fe-Pd theoretical models are shown in Fig. S16. The Gibbs free energy of H* intermediate (ΔG_{H*}) is a key parameter in predicting the theoretical nature of HER. The HER catalysts with excellent performance should process a thermoneutral nature with the ΔG_{H*} close to zero, which could facilitate the charge transfer processes for both H* adsorption and H$_2$ desorption [48,49]. As displayed in Fig. 3a, the ΔG_{H*} value of fcc Fe-Pd (−0.15 eV) was much closer to the optimal value in comparison with bcc Fe-Pd (−0.36 eV), indicating that Pd in metastable fcc phase could improve the H* adsorption, accelerate H$_2$ desorption and exhibit higher intrinsic HER activity. Additionally, the energy barrier for water dissociation was calculated to determine the rate-determining step in alkaline conditions. Fig. 3b shows the energy barriers of water decomposition and the atomic model is shown in Fig. S17. The fcc Fe-Pd exhibits a lower water adsorption energy, indicating high affinity of H$_2$O on fcc Fe-Pd. Moreover, the water dissociation energy barrier on fcc Fe-Pd (0.67 eV) decrease obviously compared with that of bcc Fe-Pd (1.14 eV), demonstrating that the fast proton supply can be achieved on the surface of metastable fcc Fe-Pd.

Fig. 3c demonstrate the projected density of states (pDOS) revealing orbital hybridization between Fe 3d and Pd 4d orbitals of different catalysts, indicating enhanced electron localization and effectiveness in metastable catalysts. The d-band centers of surface-active Pd atoms in
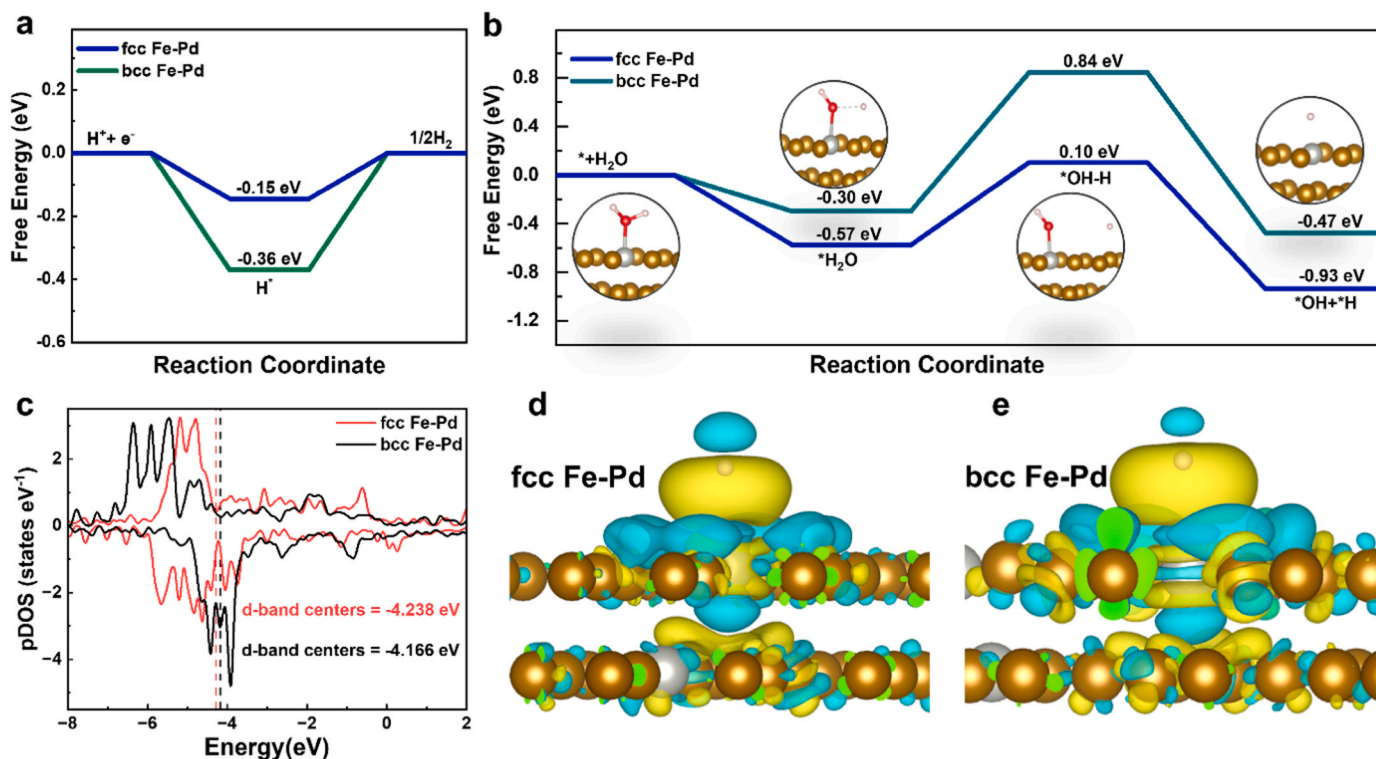
Fig. 3. Part of density functional theory (DFT) calculations from first principles. a) hydrogen free energies of systems. b) The H_2O dissociation energies. c) pDOS of different samples. d, e) differential charge density of (d) fcc Fe-Pd and (e) bcc Fe-Pd.

fcc Fe-Pd and bcc Fe-Pd are − 4.238 eV and − 4.166 eV, respectively. The calculation indicates a lower d-band centers for the metastable catalyst, illustrating the weaken of the interaction between the adsorbate and Pd active sites, leading to fast water decomposition kinetics [50–52]. Fig. 3d and e show the spatial redistribution of charge density. The yellow regions represent denote electron accumulation, and the blue regions indicate electron dissipation. The electron density distribution in the fcc Fe-Pd can be observed to shift closer to the Fe atom compared with that in the bcc Fe-Pd catalyst. This can be attributed to the different coordination environments of palladium and iron atoms in different crystal structures. In addition, a smaller number of electrons in the Pd active site can interact with H* intermediates, leading to weakened interaction between H* and Pd active site. The Pd-H bond length in the fcc Fe-Pd catalyst is 2.035 Å, which is longer than that in bcc Fe-Pd (1.846 Å), verifying the weakened hydrogen adsorption. Therefore, it is reasonable to propose that electronic structure modulation via metastable phase engineering can enhance the H_2O dissociation and H_2 desorption, thereby facilitating the HER process in alkaline media.

Utilizing flexible electrode with mechanical property and robust nanostructures has been shown to enhance electrochemical activity and durability in real water splitting processes [43,44,53,54]. Fig. 4a shows the tensile stress-strain curves of the fcc Fe-Pd and the precursor alloy. The ultimate tensile strength of the fcc Fe-Pd electrode is 545 MPa, demonstrating good mechanical property is remained after dealloying. The mechanical properties of the nanoporous layer were further measured by nanoindentation. Fig. 4b displays the different force-depth curves on fcc Fe-Pd, all curves present the similar shape, demonstrating good mechanical stability under applied load. The variation of Young's modulus and microhardness of nanoporous ribbons with indentation depth is shown in Fig. 4c, indicating that in the sandwich structure, the uncorroded substrate ensures the excellent mechanical properties of the catalyst. The corresponding scanning probe microscopy (SPM) images and 3D plots are shown in Fig. 4d and e. The area outside the indentation remains in a non-deformed state and no crack is observed nearby the indentation, indicating high bonding strength between surface

nanoporous layer and bulk substrate, thus good mechanical adhesion and excellent electrical transfer between catalyst layer and substrate can be achieved [55]. The excellent mechanical flexibility and elasticity of fcc Fe-Pd provide the possibility for feasible design of smart electrodes towards HER. The HER catalytic performance of fcc Fe-Pd under various deformation are displayed in Fig. 4f, the polarization curves obtained for fcc Fe-Pd electrode maintains similar shapes under various deformations, indicating that the bendable electrode retains a reliable current output for HER. Remarkably, as shown in Fig. 4g, the fcc Fe-Pd electrode maintains its structural integrity and catalytic activity after 100 bending cycles, revealing the high flexibility and recoverable ability. This remarkable combination of mechanical integrity and electrocatalytic performance makes fcc Fe-Pd as an excellent candidate for HER diverse application.

4. Conclusion

In summary, the metastable fcc Fe-Pd alloy is prepared by electrochemical dealloying method. The synthesized nanoporous fcc Fe-Pd exhibits an overpotential of 58 mV at 10 mA cm^{-2} and good stability at large current densities in 1 M KOH. By combining experimental analysis and DFT calculations, metastable phase engineering can tailor the coordination environment and electronic structure of Pd active site on Fe-Pd alloy, improving the hydrogen evolution by facilitating the dissociation of water molecules and the desorption of hydrogen. In addition, excellent flexibility and bonding strength ensure that the catalyst can serve as flexible electrode under various deformations.

CRediT authorship contribution statement

Cui Zhenduo: Formal analysis. **Wang Chaoyang:** Investigation, Visualization. **Li Zhangyi:** Conceptualization, Data curation, Methodology, Writing – original draft. **Jiang Hui:** Methodology. **Liang Yanqin:** Methodology. **Li Zhaoyang:** Formal analysis. **Wu Shuilin:** Formal analysis. **Zhu Shengli:** Funding acquisition, Project administration,
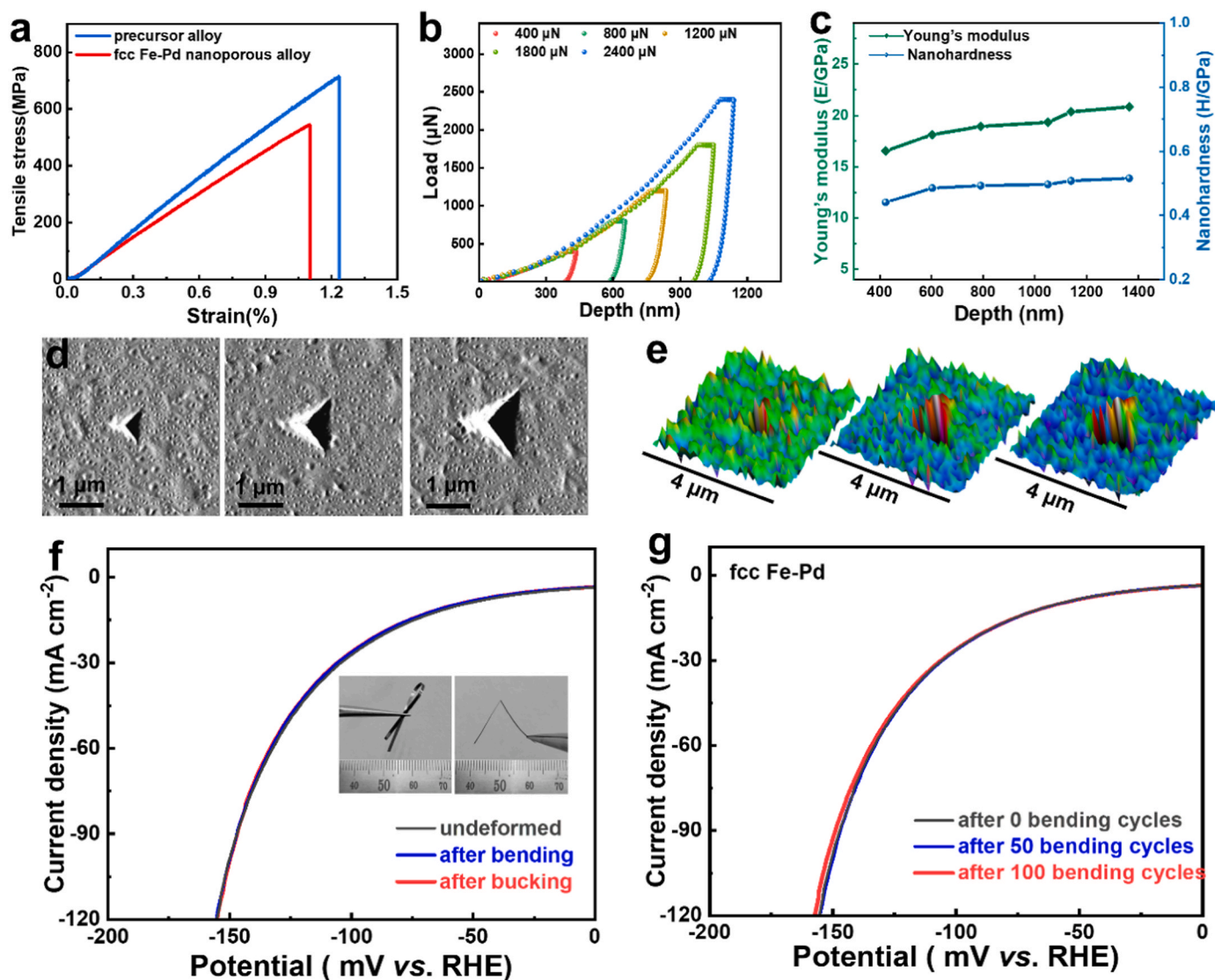
Fig. 4. Mechanical measurements of the fcc Fe-Pd ribbon and electrochemical performance under different deformation. a) The tensile stress-strain curves of nanoporous ribbon and precursor ribbon. b) The nanoindentation force-depth curves under different loads. c) Young's Modulus and Nanohardness of fcc Fe-Pd. d, e) The corresponding scanning probe microscope (SPM) images and 3D maps under different loads. f) HER catalytic performance of fcc Fe-Pd under different deformation. g) Comparison of catalytic activity of fcc Fe-Pd electrode after 50 (100) bending cycles with that without bending test.

Resources, Supervision, Validation, Writing – review & editing. **Xu Wence:** Funding acquisition, Investigation, Validation, Writing – review & editing.

Declaration of Competing Interest

The authors declare that they have no known competing financial interests or personal relationships that could have appeared to influence the work reported in this paper.

Data Availability

Data will be made available on request.

Appendix A. Supporting information

Supplementary data associated with this article can be found in the online version at doi:10.1016/j.apcatb.2023.123677.

References

[1] C. Hu, L. Zhang, J. Gong, Recent progress made in the mechanism comprehension and design of electrocatalysts for alkaline water splitting, Energ. Environ. Sci. 12 (2019) 2620–2645, https://doi.org/10.1039/c9ee01202h.

[2] W. Hong, C. Jian, G. Wang, X. He, J. Li, Q. Cai, Z. Wen, W. Liu, Self-supported nanoporous cobalt phosphosulfate electrodes for efficient hydrogen evolution reaction, Appl. Catal. B 251 (2019) 213–219, https://doi.org/10.1016/j.apcatb.2019.03.070.

[3] W. Niu, T. Moehl, P. Adams, X. Zhang, R. Lefèvre, A.M. Cruz, P. Zeng, K. Kunze, W. Yang, S.D. Tilley, Crystal orientation-dependent etching and trapping in thermally-oxidised Cu_2O photocathodes for water splitting, Energ. Environ. Sci. 15 (2022) 2002–2010, https://doi.org/10.1039/d1ee03696c.

[4] S. Zhou, J. Wang, J. Li, L. Fan, Z. Liu, J. Shi, W. Cai, Surface-growing organophosphorus layer on layered double hydroxides enables boosted and durable electrochemical freshwater/seawater oxidation, Appl. Catal. B 332 (2023) 122749, https://doi.org/10.1016/j.apcatb.2023.122749.

[5] C. Tang, R. Zhang, W. Lu, L. He, X. Jiang, A.M. Asiri, X. Sun, Fe-doped CoP nanoarray: a monolithic multifunctional catalyst for highly efficient hydrogen

generation, Adv. Mater. 29 (2016) 1602441, https://doi.org/10.1002/adma.201602441.

[6] Y. Zhu, W. Zhou, Y. Zhong, Y. Bu, X. Chen, Q. Zhong, M. Liu, Z. Shao, A perovskite nanorod as bifunctional electrocatalyst for overall water splitting, Adv. Energ. Mater. 7 (2016) 1602122, https://doi.org/10.1002/aenm.201602122.

[7] Q. Chen, B. Wei, Y. Wei, P. Zhai, W. Liu, X. Gu, Z. Yang, J. Zuo, R. Zhang, Y. Gong, Synergistic effect in ultrafine PtNiP nanowires for highly efficient electrochemical hydrogen evolution in alkaline electrolyte, Appl. Catal. B 301 (2022) 120754, https://doi.org/10.1016/j.apcatb.2021.120754.

[8] S. Niu, W.J. Jiang, T. Tang, Y. Zhang, J.H. Li, J.S. Hu, Facile and scalable synthesis of robust Ni(OH)₂ nanoplate arrays on NiAl foil as hierarchical active scaffold for highly efficient overall water splitting, Adv. Sci. 4 (2017) 1700084, https://doi.org/10.1002/advs.201700084.

[9] S. Ghosh, S.R. Kadam, S. Kolatkar, A. Neyman, C. Singh, A.N. Enyashin, R. Bar-Ziv, M. Bar-Sadan, W. Doping, in Ni₁₂P₅ as a platform to enhance overall electrochemical water splitting, ACS Appl. Mater. Interfaces 14 (2021) 581–589, https://doi.org/10.1021/acsami.1c16755.

[10] D. Zhang, J. Shi, Y. Qi, X. Wang, H. Wang, M. Li, S. Liu, C. Li, Quasi-amorphous metallic nickel nanopowder as an efficient and durable electrocatalyst for alkaline hydrogen evolution, Adv. Sci. 5 (2018) 1801216, https://doi.org/10.1002/advs.201801216.

[11] Z. Wang, J. Chen, E. Song, N. Wang, J. Dong, X. Zhang, P.M. Ajayan, W. Yao, C. Wang, J. Liu, J. Shen, M. Ye, Manipulation on active electronic states of metastable phase β-NiMoO₄ for large current density hydrogen evolution, Nat. Commun. 12 (2021) 5960, https://doi.org/10.1038/s41467-021-26256-1.

[12] S. Li, Z. Zhao, T. Ma, P. Pachfule, A. Thomas, Superstructures of organic–polyoxometalate co-crystals as precursors for hydrogen evolution electrocatalysts, Angew. Chem. Int. Ed. 61 (2021) e20211229, https://doi.org/10.1002/anie.202112298.

[13] Z.Y. Yu, Y. Duan, X.Y. Feng, X. Yu, M.R. Gao, S.H. Yu, Clean and affordable hydrogen fuel from alkaline water splitting: past, recent progress, and future prospects, Adv. Mater. 33 (2021) 2007100, https://doi.org/10.1002/adma.202007100.

[14] S. Wang, B. Xu, W. Huo, H. Feng, X. Zhou, F. Fang, Z. Xie, J.K. Shang, J. Jiang, Efficient FeCoNiCuPd thin-film electrocatalyst for alkaline oxygen and hydrogen evolution reactions, Appl. Catal. B 313 (2022) 121472, https://doi.org/10.1016/j.apcatb.2022.121472.

[15] A. Janssen, Q.N. Nguyen, Y. Xia, Colloidal metal nanocrystals with metastable crystal structures, Angew. Chem. Int. Ed. 60 (2021) 12192–12203, https://doi.org/10.1002/anie.202017076.

[16] W. Yan, Y. Shen, C. An, L. Li, R. Si, C. An, FeOx clusters decorated hcp Ni nanosheets as inverse electrocatalyst to stimulate excellent oxygen evolution performance, Appl. Catal. B 284 (2021) 119687, https://doi.org/10.1016/j.apcatb.2020.119687.

[17] X. Tan, S. Geng, Y. Ji, Q. Shao, T. Zhu, P. Wang, Y. Li, X. Huang, Closest packing polymorphism interfaced metastable transition metal for efficient hydrogen evolution, Adv. Mater. 32 (2020) 2002857, https://doi.org/10.1002/adma.202002857.

[18] T. Zhu, C. Liu, X. Tan, B. Huang, G.-Q. Bian, Q. Shao, S. Bai, Y. Qian, Y. Li, X. Huang, Se-incorporation stabilizes and activates metastable MoS₂ for efficient and cost-effective water gas shift reaction, ACS Nano 13 (2019) 11303–11309, https://doi.org/10.1021/acsnano.9b04444.

[19] P. Chen, T.-Y. Xiao, Y.-H. Qian, S.-S. Li, S.-H. Yu, A. Nitrogen-Doped Graphene/Carbon, Nanotube nanocomposite with synergistically enhanced electrochemical activity, Adv. Mater. 25 (2013) 3192–3196, https://doi.org/10.1002/adma.201300515.

[20] Z. Zhang, G. Liu, X. Cui, B. Chen, Y. Zhu, Y. Gong, F. Saleem, S. Xi, Y. Du, A. Borgna, Z. Lai, Q. Zhang, B. Li, Y. Zong, Y. Han, L. Gu, H. Zhang, Crystal phase and architecture engineering of lotus-thalamus-shaped Pt-Ni anisotropic superstructures for highly efficient electrochemical hydrogen evolution, Adv. Mater. 30 (2018) 1801741, https://doi.org/10.1002/adma.201801741.

[21] Y. Liu, M. Chi, V. Mazumder, K.L. More, S. Soled, J.D. Henao, S. Sun, Composition-controlled synthesis of bimetallic PdPt nanoparticles and their electro-oxidation of methanol, Chem. Mater. 23 (2011) 4199–4203, https://doi.org/10.1021/cm2014785.

[22] Y. Cao, L. Guo, M. Dan, D.E. Doronkin, C. Han, Z. Rao, Y. Liu, J. Meng, Z. Huang, K. Zheng, P. Chen, F. Dong, Y. Zhou, Modulating electron density of vacancy site by single Au atom for effective CO₂ photoreduction, Nat. Commun. 12 (2021) 1675, https://doi.org/10.1038/s41467-021-21925-7.

[23] S. Zhou, Y. Liu, J. Shi, J. Li, W. Cai, Regulating the electronic structure of metal–organic frameworks via ion-exchanged Ir dispersion for robust overall water splitting, Chem. Commun. 59 (2023) 14459–14462, https://doi.org/10.1039/d3cc04990f.

[24] Q. Zeng, J. Song, P. Cui, H. Liu, L. Tian, D. Chen, J. Yang, Optimizing lattice strain and electron effect of ultrathin platinum nanoshells through core–shell construction toward superior electrocatalytic hydrogen evolution, Ind. Eng. Chem. Res. 61 (2022) 7529–7536, https://doi.org/10.1021/acs.iecr.1c04793.

[25] Y. Zhou, Y. Shen, X. Luo, G. Liu, Y. Cao, Boosting activity and selectivity of glycerol oxidation over platinum–palladium–silver electrocatalysts via surface engineering, Nanoscale Adv. 2 (2020) 3423–3430, https://doi.org/10.1039/d0na00252f.

[26] Q. Zeng, S. Tian, H. Liu, L. Xu, P. Cui, D. Chen, J. Wang, J. Yang, Fine AgPd nanoalloys achieving size and ensemble synergy for high-efficiency CO₂ to CO electroreduction, Adv. Funct. Mater. 33 (2023) 2307444, https://doi.org/10.1002/adfm.202307444.

[27] D. Liu, S. Tian, Y. Zhang, C. Hu, H. Liu, D. Chen, L. Xu, J. Yang, Ultrafine SnPd nanoalloys promise high-efficiency electrocatalysis for ethanol oxidation and

oxygen reduction, ACS Appl. Energ. Mater. 6 (2023) 1459–1466, https://doi.org/10.1021/acsaem.2c03355.

[28] C. Wang, Z. Li, S. Zhu, Y. Liang, Z. Cui, S. Wu, C. Qin, S. Luo, A. Inoue, Dual-phase nanostructuring as a route to flexible nanoporous metals with outstanding comprehensive mechanical properties, Sci. China Mater. 64 (2021) 2289–2304, https://doi.org/10.1007/s40843-020-1606-4.

[29] X. Yang, W. Xu, S. Cao, S. Zhu, Y. Liang, Z. Cui, X. Yang, Z. Li, S. Wu, A. Inoue, L. Chen, An amorphous nanoporous PdCuNi-S hybrid electrocatalyst for highly efficient hydrogen production, Appl. Catal. B 246 (2019) 156–165, https://doi.org/10.1016/j.apcatb.2019.01.030.

[30] S. Anantharaj, S. Noda, Amorphous catalysts and electrochemical water splitting: an untold story of harmony, Small 16 (2019) 1905779, https://doi.org/10.1002/smll.201905779.

[31] J. Zhang, Q. Zhang, X. Feng, Support and interface effects in water-splitting electrocatalysts, Adv. Mater. 31 (2019) 1808167, https://doi.org/10.1002/adma.201808167.

[32] S. Anantharaj, P.E. Karthik, S. Noda, The significance of properly reporting turnover frequency in electrocatalysis research, Angew. Chem. Int. Ed. 60 (2021) 23051–23067, https://doi.org/10.1002/anie.202110352.

[33] S.I. Perez Bakovic, P. Acharya, M. Watkins, H. Thornton, S. Hou, L.F. Greenlee, Electrochemically active surface area controls HER activity for FeₓNi₁₀₀₋ₓ films in alkaline electrolyte, J. Catal. 394 (2021) 104–112, https://doi.org/10.1016/j.jcat.2020.12.037.

[34] D. Voiry, M. Chhowalla, Y. Gogotsi, N.A. Kotov, Y. Li, R.M. Penner, R.E. Schaak, P. S. Weiss, Best practices for reporting electrocatalytic performance of nanomaterials, ACS Nano 12 (2018) 9635–9638, https://doi.org/10.1021/acsnano.8b07700.

[35] Y.K. Chen, J.Y. Yu, J. Jia, F. Liu, Y.W. Zhang, G.W. Xiong, R.T. Zhang, R.Q. Yang, D.H. Sun, H. Liu, W.J. Zhou, Metallic Ni₃Mo₃N porous microrods with abundant catalytic sites as efficient electrocatalyst for large current density and superstability of hydrogen evolution reaction and water splitting, Appl. Catal. B 272 (2020) 118956, https://doi.org/10.1016/j.apcatb.2020.118956.

[36] Y. Jin, G. Xi, R. Li, Z.-A. Li, X.-B. Chen, T. Zhang, Nanoporous metallic-glass electrocatalysts for highly efficient oxygen evolution reaction, J. Alloy. Comp. 852 (2021) 156876, https://doi.org/10.1016/j.jallcom.2020.156876.

[37] Y. Jin, R. Li, H. Xu, X.-B. Chen, T. Zhang, A new strategy to fabricate nanoporous iron-based metallic glasses: selective phase tailoring of amorphous-nanocrystalline composite alloys through electrochemical dissolution, Scr. Mater. 133 (2017) 14–18, https://doi.org/10.1016/j.scriptamat.2017.01.029.

[38] R. Li, X. Liu, R. Wu, J. Wang, Z. Li, K.C. Chan, H. Wang, Y. Wu, Z. Lu, Flexible honeycombed nanoporous/glassy hybrid for efficient electrocatalytic hydrogen generation, Adv. Mater. 31 (2019) 1904989, https://doi.org/10.1002/adma.201904989.

[39] M. Qu, Y. Jiang, M. Yang, S. Liu, Q. Guo, W. Shen, M. Li, R. He, Regulating electron density of NiFe-P nanosheets electrocatalysts by a trifle of Ru for high-efficient overall water splitting, Appl. Catal. B 263 (2020) 118324, https://doi.org/10.1016/j.apcatb.2019.118324.

[40] G. Hu, F. Nitze, E. Gracia-Espino, J. Ma, H.R. Barzegar, T. Sharifi, X. Jia, A. Shchukarev, L. Lu, C. Ma, G. Yang, T. Wågberg, Small palladium islands embedded in palladium–tungsten bimetallic nanoparticles form catalytic hotspots for oxygen reduction, Nat. Commun. 5 (2014) 5253, https://doi.org/10.1038/ncomms6253.

[41] Y. Tan, F. Zhu, H. Wang, Y. Tian, A. Hirata, T. Fujita, M. Chen, Noble-metal-free metallic glass as a highly active and stable bifunctional electrocatalyst for water splitting, Adv. Mater. Interfaces 4 (2017) 1601086, https://doi.org/10.1002/admi.201601086.

[42] D. Liu, Q. Zeng, C. Hu, H. Liu, D. Chen, Y. Han, L. Xu, J. Yang, Core–shell CuPd@NiPd nanoparticles: coupling lateral strain with electronic interaction toward high-efficiency electrocatalysis, ACS Catal. 12 (2022) 9092–9100, https://doi.org/10.1021/acscatal.2c02274.

[43] Z.-X. Cai, H. Goou, Y. Ito, T. Tokunaga, M. Miyauchi, H. Abe, T. Fujita, Nanoporous ultra-high-entropy alloys containing fourteen elements for water splitting electrocatalysis, Chem. Sci. 12 (2021) 11306–11315, https://doi.org/10.1039/d1sc01981c.

[44] J. Chen, G. Xia, P. Jiang, Y. Yang, R. Li, R. Shi, J. Su, Q. Chen, Active and durable hydrogen evolution reaction catalyst derived from Pd-doped metal–organic frameworks, ACS Appl. Mater. Interfaces 8 (2016) 13378–13383, https://doi.org/10.1021/acsami.6b01266.

[45] X. Tian, P. Zhao, W. Sheng, Hydrogen evolution and oxidation: mechanistic studies and material advances, Adv. Mater. 31 (2019) 1818266, https://doi.org/10.1002/adma.201808066.

[46] Y. Lin, Z. Tian, L. Zhang, J. Ma, Z. Jiang, B.J. Deibert, R. Ge, L. Chen, Chromium-ruthenium oxide solid solution electrocatalyst for highly efficient oxygen evolution reaction in acidic media, Nat. Commun. 10 (2019) 162, https://doi.org/10.1038/s41467-018-08144-3.

[47] J. Shi, H. He, Y. Guo, F. Ji, J. Li, Y. Zhang, C. Deng, L. Fan, W. Cai, Enabling high-efficiency ethanol oxidation on NiFe-LDH via deprotonation promotion and absorption inhibition, J. Energ. Chem. 85 (2023) 76–82, https://doi.org/10.1016/j.jechem.2023.06.011.

[48] S. Lu, H.L. Huynh, F. Lou, K. Guo, Z. Yu, Single transition metal atom embedded antimonene monolayers as efficient trifunctional electrocatalysts for the HER, OER and ORR: a density functional theory study, Nanoscale 13 (2021) 12885–12895, https://doi.org/10.1039/d1nr02235k.

[49] S. Chen, H. Wang, S. Lu, Y. Xiang, Monolayer MoS2 film supported metal electrocatalysts: a DFT study, RSC Adv. 6 (2016) 107836–107839, https://doi.org/10.1039/c6ra23995a.

[50] W. Xu, G. Fan, S. Zhu, Y. Liang, Z. Cui, Z. Li, H. Jiang, S. Wu, F. Cheng, Electronic structure modulation of nanoporous cobalt phosphide by carbon doping for alkaline hydrogen evolution reaction, Adv. Funct. Mater. 31 (2021) 2017333, https://doi.org/10.1002/adfm.202107333.

[51] Z. Li, L. Yu, C. Milligan, T. Ma, L. Zhou, Y. Cui, Z. Qi, N. Libretto, B. Xu, J. Luo, E. Shi, Z. Wu, H. Xin, W.N. Delgass, J.T. Miller, Y. Wu, Two-dimensional transition metal carbides as supports for tuning the chemistry of catalytic nanoparticles, Nat. Commun. 9 (2018) 5258, https://doi.org/10.1038/s41467-018-07502-5.

[52] B. Zhang, F. Yang, X. Liu, N. Wu, S. Che, Y. Li, Phosphorus doped nickel-molybdenum aerogel for efficient overall water splitting, Appl. Catal. B 298 (2021) 120494, https://doi.org/10.1016/j.apcatb.2021.120494.

[53] Y. Tan, H. Wang, P. Liu, C. Cheng, F. Zhu, A. Hirata, M. Chen, 3D nanoporous metal phosphides toward high-efficiency electrochemical hydrogen production, Adv. Mater. 28 (2016) 2951–2955, https://doi.org/10.1002/adma.201505875.

[54] R.Q. Yao, H. Shi, W.B. Wan, Z. Wen, X.Y. Lang, Q. Jiang, Flexible Co–Mo–N/Au electrodes with a hierarchical nanoporous architecture as highly efficient electrocatalysts for oxygen evolution reaction, Adv. Mater. 32 (2020) 1907214, https://doi.org/10.1002/adma.201907214.

[55] C. Wang, S. Zhu, Y. Liang, Z. Cui, S. Wu, C. Qin, S. Luo, A. Inoue, Understanding the macroscopical flexibility/fragility of nanoporous Ag: depending on network connectivity and micro-defects, J. Mater. Sci. Technol. 53 (2020) 91–101, https://doi.org/10.1016/j.jmst.2020.04.010.